

Mineralogical and Physico-chemical Properties of Halloysite-bearing Slip Surface Material From a Landslide During the 2018 Eastern Iburi Earthquake, Hokkaido

Jun Kameda (✉ kameda@sci.hokudai.ac.jp)

Department of Earth and Planetary Sciences, Faculty of Science, Hokkaido University, N10W8, Kita-ku, Sapporo, 060-0810 Japan

Research article

Keywords: 2018 Hokkaido Eastern Iburi earthquake, shallow landslide, liquefaction, halloysite

Posted Date: December 1st, 2020

DOI: <https://doi.org/10.21203/rs.3.rs-113709/v1>

License:  This work is licensed under a Creative Commons Attribution 4.0 International License.

[Read Full License](#)

1 **Mineralogical and physico-chemical properties of**
2 **halloysite-bearing slip surface material from a landslide**
3 **during the 2018 Eastern Iburi earthquake, Hokkaido**

4 Jun Kameda ¹

5 Corresponding author

6 Email: kameda@sci.hokudai.ac.jp

7

8 (Institutional addresses)

9 ¹ Department of Earth and Planetary Sciences, Faculty of Science, Hokkaido University,
10 N10W8, Kita-ku, Sapporo, 060-0810 Japan

11

12 **Abstract**

13 Destructive landslides were triggered by the 6.7 M_w Eastern Iburi earthquake that struck
14 southern Hokkaido, Japan on 6 September 2018. Heavy rainfall on 4 September in addition to
15 intermittent rainfall around the Iburi Tobu area saturated and weakened altered volcanoclastic
16 soils containing halloysite minerals, making them susceptible to failure because of the
17 earthquake's strong ground motion. The landslides exhibited laminar flow behavior, with long
18 runouts along gentle hill slopes. This study investigated the mineralogical and physicochemical
19 properties of the halloysite-bearing slip surface material with the aim of understanding

20 weakening and post-failure behaviors during the landslides. Halloysite in the slip surface had
21 irregular-to-hollow-spherical morphology with higher mesopore volumes than tubular
22 halloysite, which is related to a high capacity for water retention after rainfall. To reproduce
23 possible chemical changes in the slip surface during rainfall, the sample was immersed in
24 varying amounts of rainwater; solution pH increased and ionic strength decreased with
25 increasing water content. These findings, alongside electrophoretic analysis, suggest that
26 rainwater infiltration could have increased the absolute zeta potential value of the slip surface
27 material. It is suggested that rainfall before the earthquake enhanced the colloidal stability of
28 halloysite particles within the slip surface, owing to an increase in electrostatic repulsion. This
29 decreased the material's cohesive strength, which might have led to destabilization of the slope
30 during ground shaking generated by the earthquake, and subsequent high-mobility flow after
31 failure.

32

33 **Keywords**

34 2018 Hokkaido Eastern Iburi earthquake, shallow landslide, liquefaction, halloysite

35

36

37 **1 Introduction**

38 The Eastern Iburi earthquake ($M_w = 6.7$) occurred at 3:07 AM (local time) on 6 September
39 2018 in southern Hokkaido, Japan (Fig. 1a). The resulting strong ground motion (with a
40 maximum intensity of 7 on the Japan Meteorology Agency [JMA] intensity scale) caused hill
41 slopes near the epicenter to fail suddenly. These slopes are widely covered by volcanic soils
42 that originated from nearby volcanoes such as Tarumai, Eniwa, and Shikotsu (Yamada 1958;
43 Katsui 1959; Furukawa and Nakagawa 2000). Around 6000 landslides occurred in the area
44 (Yamagishi and Yamazaki 2018), with many of the recorded landslides being shallow and
45 exhibiting features of liquefaction, such as long runouts of debris on relatively gentle slopes
46 ($< \sim 30^\circ$; Osanai et al. 2019; Kasai and Yamada 2019). Field surveys revealed that the basal part
47 of the volcanic soils acted as the principal slip surface (Chigira et al. 2018; Kameda et al. 2019;
48 Ito et al. 2020); these soils characteristically contain the mineral halloysite (Chigira et al. 2018;
49 Kameda et al. 2019).

50 Halloysite is a typical alteration product in pyroclastic deposits, and occurs after allophane
51 in the weathering sequence (Wada 1977, 1980; Parfitt et al. 1983). Halloysite exhibits various
52 morphologies in nature; the most common form is elongated tubes, but spheroidal and platy
53 halloysite has also been observed (Askenasy, 1973; Joussein et al., 2005). Halloysite often
54 occurs on the slip surface of landslides in volcanic areas of Japan (Chigira and Yokoyama 2005;

55 Chigira et al. 2012), Indonesia (Nakano et al. 2013), and New Zealand (Moon 2016; Kluger et
56 al. 2017). Spherical halloysite is most common in such cases (Smalley, 1980). In general,
57 halloysite-bearing soils and deposits exhibit higher peak as well as residual friction angles than
58 those that contain platy clay minerals, which suggests that they may be stable on steep slopes
59 (Moon 2016). However, the material also exhibits high sensitivity (i.e., loss of strength by
60 remolding), which possibly causes high mobility flows after failure (Moon 2016). Moon (2016)
61 also suggested the important effects of physico-chemical interactions between the clay surfaces
62 and cations in pore water on the rheological properties of halloysite-bearing soils. Rheological
63 experiments have demonstrated that the flow properties of halloysite suspensions depend on
64 the solution chemistry (pH and NaCl concentration), which modify the halloysite surface
65 properties and influence the resulting association types of individual particles (Theng and Wells
66 1995). Recently, Kluger et al. (2017) observed halloysite with a unique morphology in a tephra
67 layer involved in a flow slide, and suggested that weak interparticle interactions contributed to
68 the high sensitivity of the material. These findings indicate that evaluation of the surface
69 physico-chemical properties of the constituent halloysite mineral and their changes in response
70 to contacting pore water is key to understanding the mechanism of landslide initiation, as well
71 as their runout behavior in volcanic areas. This study analyzed the mineralogical and physico-
72 chemical properties of the slip surface material from a landslide triggered by the Eastern Iburi

73 earthquake, and used the results to discuss the possible weakening process of the material.

74

75 **2 Studied landslide**

76 Kameda et al. (2019) described the studied landslide in detail. The site is located in the
77 Tomisato district of Atsuma town, southern Hokkaido (Figs 1a and b). The hill had a slope of
78 $\sim 20^\circ$, dipping westward; the hill largely collapsed, and slid downward with a runout distance
79 of ~ 100 m (Fig. 1c). The collapsed slope was covered by clayey striated mud (Fig. 1d), which
80 was often wet during field surveys. The scarp of the landslide exhibited a stratigraphic sequence
81 of pyroclastic deposits supplied from the Tarumai Volcano on a basement of Neogene marine
82 beds: Ta-b (AD1667; Nakagawa et al. 2018), Ta-c (ca. 2.5 ka), and Ta-d (ca. 9 ka) deposits with
83 two inter-bedded andosol layers (Fig. 1e). A clayey layer, several tens of centimeters thick and
84 resembling the striated mud on the slope, was observed at the base of the scarp (i.e., the Ta-d
85 layer). Based on field observations as well as the results of laboratory measurements, the clayey
86 layer was found to act as a slip surface during the landslide. X-ray diffraction analysis revealed
87 that the slip surface principally contained halloysite (Kameda et al. 2019). Surveys of several
88 other locations indicated that many of the landslides around this area were triggered by the
89 earthquake in a similar manner (Kameda et al. 2019).

90

91 **3 Methods**

92 **3.1 X-ray diffraction (XRD) analysis**

93 Previous XRD analysis of the clay-size fraction of the slip surface material has revealed the
94 occurrence of halloysite (Kameda et al. 2019). This study additionally conducted bulk XRD to
95 quantify the halloysite content. The bulk powder sample, mixed with corundum (AX-5H,
96 Hinomoto Kenmazai Co.) as an internal standard at a weight ratio of 4:1, was mounted on a
97 glass holder by side loading to minimize the development of a preferred alignment of the clay
98 minerals. XRD patterns were recorded using a MAC Science MX-Labo with monochromatized
99 CuK α radiation at 40 kV and 30 mA, 1° divergence and anti-scattering slits, and a 0.15-mm
100 receiving slit in continuous scan mode at a rate of 1° 2 θ per minute. The weight contents of
101 crystalline phases such as halloysite and other minerals were determined using the reference
102 intensity ratio (RIR) (Hillier 2000). The RIR value I/I_{cor} of the halloysite peak at ~20°
103 ($d = 4.4 \text{ \AA}$), relative to corundum, was determined to be 0.225 from the measurement of a 50:50
104 mixture using a commercially available standard sample (Halloysite nanoclay, Sigma-Aldrich).
105 The standard halloysite was a synthetic powder with tubular morphology (50 nm outer diameter
106 and 15 nm inner diameter). In the following, the standard sample was not further purified before
107 use.

108 **3.2 Transmission electron microscopy (TEM) observation**

109 The morphological features of the halloysite-bearing slip surface material were observed by
110 TEM (JEM-2100F, Jeol). For TEM observation, the fine fraction of the sample was separated
111 by centrifugation, and dispersed on a holey carbon film.

112 **3.3 Specific surface area and pore size distribution by N₂ adsorption–desorption** 113 **analysis**

114 The specific surface area and pore size distribution (PSD) of the samples were measured
115 using an automated sorption analyser (Autosorb, Quantachrome Instruments). Prior to
116 measurement, the samples were dried and degassed at 105 °C for 15 h under vacuum. Nitrogen
117 adsorption–desorption assessed at 77 K provided isotherms for Brunauer–Emmett–Teller
118 (BET) analysis to determine the surface areas. The adsorption isotherm was also provided for
119 PSD analysis based on the Barrett–Joyner–Halenda (BJH) method (Barrett et al. 1951). For
120 comparison, we also analyzed the standard samples of halloysite and allophane (Sekado-2,
121 Shinagawa General Co., Ltd.). The standard allophane was a purified sample collected from
122 Kitakami pumice, Iwate, Japan. The allophane particles has a hollow spherical morphology
123 with ~5 nm outer diameter and ~3 nm inner diameter (Brigattie et al. 2006).

124 **3.4 Water adsorption–desorption measurement**

125 The adsorption and desorption of water were measured using an automated sorption
126 analyser (N-VP, MicrotracBEL). Prior to measurement, the bulk powder sample was dried
127 and degassed at 105 °C for 15 h under vacuum. The water adsorption–desorption isotherm
128 was obtained at 25 °C for relative pressures, P/P_0 , ranging from 0 to 0.9.

129 **3.5 Immersion of the slip surface material in distilled water and rainwater**

130 To simulate possible changes of the solution chemistry of pore water within the slip surface
131 during rainfall, samples were immersed in rainwater and distilled water (FUJIFILM Wako Pure
132 Chemicals Co.) at different solid/water weight ratios (S/W), and pH and electrical conductivity
133 (EC) measurements of the resulting solutions were taken after 24 h. The rainwater was sampled
134 on 30 August 2020 at Atsuma town in the same season as when the disaster occurred. Before
135 the experiments, solid contaminants were removed from the rainwater by filtering it through a
136 0.45 µm filter attached to the tip of a syringe.

137 **3.6 Zeta potential and dynamic light scattering analysis**

138 For electrophoretic measurement, samples were centrifuged to separate the >2 µm clay
139 fraction. Samples were then dialyzed using distilled water until the conductivity of the outside
140 solution became ~2.0 µS/cm. The electrophoretic mobility μ of the sample was measured
141 using a Zetasizer Nano (Malvern), and the zeta potential ζ was obtained as follows based on

142 the Smoluchowski relationship (Smoluchowski 1921):

143
$$\mu = \frac{\varepsilon_0 \varepsilon \zeta}{\eta}, (1)$$

144 where ε_0 is the vacuum permittivity, ε is the dielectric constant of water, and η is the
145 viscosity of the solution. The pH of the solution was adjusted by adding HCl and NaOH (0.01
146 N) solutions with background ionic strength of 10^{-2} , 10^{-3} , and 10^{-4} M NaCl.

147 The hydrodynamic diameter of the particles (spherical equivalent) was measured using the
148 same apparatus as that used for electrophoretic mobility measurement (Zetasizer Nano), which
149 used dynamic light scattering after 24 h of the sample being immersed in solutions of different
150 ionic strengths (10^{-4} –0.5 M NaCl).

151

152 **4 Results**

153 Figure 2 shows the XRD pattern of the slip surface material with a corundum internal
154 standard. The pattern shows peaks for halloysite, but for plagioclase and clinopyroxene. The
155 RIR method yielded halloysite, plagioclase, and clinopyroxene contents of ~40%, ~4%, and
156 ~4%, respectively, with the remainder (~50%) being amorphous low-crystalline materials such
157 as volcanic glass.

158 The TEM observation revealed that halloysite in the slip surface was mostly irregularly
159 shaped, but some particles appeared as hollow spheres with a wall thickness of several tens of

160 nanometers (Fig. 3). The particles often formed large aggregates several hundreds of
161 nanometers in diameter. Tubular halloysite was rarely observed. Wada and Mizota (1979) found
162 that halloysite in the Ta-d layer (i.e., strata identical to the slip surface) comprised particles
163 shaped like wood shavings, but this was not observed here. Therefore, the morphological
164 features of halloysite possibly depend on location, even within a given stratum.

165 Figure 4a shows the N₂ adsorption–desorption isotherms of the three samples; Table 1
166 summarizes the specific surface area and total pore volume determined from these isotherms.
167 The total pore volumes, estimated from the amounts of adsorbed N₂ at a relative pressure of
168 $P/P_0 = 0.99$, are almost the same for the three samples (0.35–0.39 m³/g). The specific surface
169 areas of the standard halloysite and allophane are 49 and 285 m²/g, respectively, consistent with
170 previous results for the same samples (Saeki et al. 2010; Em et al. 2020), whereas the slip
171 surface material exhibited an intermediate value between the two standard samples (118 m²/g).
172 The standard halloysite showed a reversible Type II isotherm from the classification of The
173 International Union of Pure and Applied Chemistry (IUPAC) (Sing 1985), suggesting that the
174 sample contained predominantly macropores (>50 nm), which is also supported by the PSD
175 curve derived from the BJH method (Fig. 4b). The standard allophane exhibited a Type IV
176 isotherm with some hysteresis indicating the presence of mesopores (Iyoda et al. 2012). The
177 PSD indicates the occurrence of mesopores with a peak around 4–5 nm in size, possibly

178 corresponding to the inter-particle and inter-microaggregate spaces of allophane particles
179 (Wang et al. 2020). Micropores (<2 nm) due to the crust of allophane particles may also have
180 contributed to the increased amounts of adsorbed N₂ compared with the other samples (Wada
181 1989; Tomura et al. 1997). The adsorption isotherm of the slip surface material resembles that
182 of the standard halloysite, but shows a clear hysteresis loop indicating the presence of
183 mesopores. The PSD shows higher volumes of mesopores (ranging from ~2 to 40 nm) than the
184 standard halloysite, possibly owing to the different morphologies of the two samples (i.e.,
185 tubular halloysite in the standard sample and hollow spheres in the slip surface sample).

186 Figure 5a shows water adsorption–desorption isotherms of the three samples. Allophane
187 showed the greatest water adsorbed with two step rises of the isotherm at $P/P_0 = 0–0.3$ and $0.6–$
188 0.9 ; these are possibly attributable to capillary condensation of water at micropores and
189 mesopores, respectively (Tomura et al. 1997; Suzuki et al. 2001). Such a step-like rise was not
190 shown by the slip surface material or the standard halloysite. The adsorbed amounts of water
191 on the slip surface material were approximately twice as large as those of the standard halloysite,
192 possibly due to the presence of mesopores, as represented by a larger hysteresis loop. This
193 feature may also have contributed to the higher water retention capacity of the slip surface
194 material in comparison with the tubular halloysite.

195 Figure 6 shows the results of immersion tests. The pH of the rainwater increased as the

196 amount of water used for immersion increased, rising from ~ 6.3 at $S/W = 0.65$ to ~ 7.0 at S/W
197 $= 0.2$. In contrast, the EC of the solution decreased as the amount of water increased, from 60
198 $\mu\text{S}/\text{cm}$ at $S/W = 0.65$ to 30 $\mu\text{S}/\text{cm}$ at $S/W = 0.2$. These values correspond to $\sim 5.0 \times 10^{-4}$ and
199 $\sim 0.25 \times 10^{-4}$ M NaCl, respectively. Using distilled water obtained almost similar results (Fig.
200 6).

201 Figures 7 shows the results of electrophoretic analysis of the slip surface material. For
202 comparison, standard allophane and halloysite were also analyzed (Fig. 7a). The zeta potential
203 of allophane increased from -35 mV at $\text{pH} = \sim 12$ to $+30$ mV at $\text{pH} = \sim 2$, with a point of zero
204 charge (PZC) at $\text{pH} = \sim 6$. The zeta potential of the standard halloysite increased from -45 mV
205 at $\text{pH} = \sim 10$ to $+10$ mV at $\text{pH} = \sim 2$, with a PZC at $\text{pH} = \sim 3$. These results are largely consistent
206 with the literature (Vergaro et al. 2010; Kawachi et al. 2013). The zeta potential of the slip
207 surface material largely behaved in a similar manner to the standard halloysite, but differed at
208 lower pH. The reason for this discrepancy is uncertain, but could be due to the samples' differing
209 morphological features (as described above). We also examined the dependence of ionic
210 strength on the zeta potential of the slip surface material. Figure 7b indicates that the zeta
211 potential decreased (an increase in absolute value) as ionic strength decreased from 10^{-2} to 10^{-4}
212 M particularly at $\text{pH} > 3.5$.

213 The hydrodynamic diameter of the particles was ~ 1000 nm below 5.0×10^{-4} M NaCl (Fig.

214 8). It initially increased up to 3000 nm as ionic strength increased, then dropped to ~2000 nm
215 at < 0.05 M.

216

217 **5 Discussion**

218 The studied landslide was eventually triggered by the earthquake, but heavy rainfall due to
219 a typhoon and intermittent rainfall over several weeks before the earthquake saturated and
220 weakened the volcanic soil on the slope. Halloysite in the slip surface had an irregular-to-
221 hollow-spherical morphology with higher mesopore volumes than the tubular halloysite, which
222 may have contributed to its high water retention capacity, and thus the soil containing such
223 halloysite may have been wet for a long period after rainfall. The immersion test results suggest
224 that successive rainwater infiltration of the slip surface could have modified the pore water
225 chemistry, with pH increasing and ionic strength decreasing (Fig. 6). The zeta potential
226 measurements (Fig. 7) suggest that both these changes enhanced the stability of colloidal
227 halloysite particles as the absolute values of zeta potential increased. This implies a qualitative
228 decrease in the soil's cohesive strength (Plaza et al. 2018).

229 Applying the classic theory of Derjaguin–Landau–Verwey–Overbeek (DLVO theory) for
230 colloidal stability, I attempted to estimate the interparticle potential of the halloysite particles.
231 The potential energy can be obtained by the sum of the electrostatic double layer (i.e., repulsive

232 energy V^{EL}) and Lifshitz–van der Waals (attractive energy V^{LW}) interactions as a function of
233 distance between the particles s :

234 $V_T = V^{EL}(s) + V^{LW}(s)$. (2)

235 For spherical particles, these energies can be expressed as follows (Duran et al. 1998;
236 Israeravili 2012):

237 $V^{EL}(s) = 2\pi\epsilon_0\epsilon a\zeta^2 \ln(1 + \exp(-\kappa s))$, (3)

238 $V^{LW}(s) = \frac{-A}{6} \left(\frac{2a^2}{s(4a+s)} + \frac{2a^2}{(2a+s)^2} + \ln \left(\frac{s(4a+s)}{(2a+s)^2} \right) \right)$, (4)

239 where a is the particle radius, A is the Hamaker constant, and κ is the reciprocal of the
240 Debye length (double-layer thickness). Applying $a = 1000$ nm from the dynamic light
241 scattering experiment (Fig. 8) and $A = 2.5 \times 10^{-20}$ J (a silicate surface typically shows $A = \sim$
242 $(1-5) \times 10^{-20}$ J; Lagaly 2006), the interparticle potentials (in kT where k is the Boltzmann
243 constant and T is temperature in kelvin) can be plotted as in Figure 9.

244 The interparticle potential increased as ionic strength decreased at constant zeta potential
245 (-35 mV; Fig. 9a). For a constant ionic strength, the interparticle potential increased as the
246 zeta potential decreased (an increase in absolute value; Fig. 9b). These results also suggest
247 that increasing pH and decreasing ionic strength due to increasing rainwater infiltration
248 enhanced the interparticle potential, thereby causing a loss in cohesive strength of the
249 material. Kameda et al. (2019) reported that natural water content during a field survey was

250 ~150%, which corresponds to a S/W of ~0.67 in Figure 3. The water content should, however,
251 vary depending on the weather conditions, and will be less during the dry season.

252 Interestingly, if the main ion species in the pore water are assumed to be Na^+ and Cl^- , the EC
253 corresponds to a concentration of $\sim 5.0 \times 10^{-4}$ M (Figure 6), above which the particle diameter
254 increases quickly, owing to coagulation (Figure 8; i.e., the critical coagulation concentration;
255 Van Olphen 1977). This suggests that the cohesive strength of the materials increases quickly
256 if the water content decreases from the state described above. In this case, heavy rainfall due
257 to Typhoon Jebi (on 4 September) as well as intermittent rainfall over a period of several
258 weeks in the summer of 2018 likely saturated the slip surface. As discussed above, this might
259 have reduced its cohesive strength, and facilitated destabilization by coseismic ground motion
260 and high-mobility flow after failure.

261 Electrophoretic measurement also revealed that the PZC of allophane is at $\text{pH} = \sim 6.0$ and
262 the absolute zeta potential value is much smaller than that of the slip surface material at
263 neutral pH (Fig. 7), suggesting that the cohesive strength of the upper strata containing
264 allophane is larger than those containing halloysite. This may be one reason why halloysite
265 has often been observed in the slip surfaces of the landslides in volcanic areas (Chigira and
266 Yokoyama 2005; Chigira et al. 2012; Nakano et al. 2013; Moon 2016; Kluger et al. 2017).
267 The alteration of volcanoclastic sediments first produces allophane, which is successively

268 replaced by halloysite (Wada 1977; 1980; Parfitt et al. 1983), possibly due to dissolution–
269 recrystallization transformation processes (Inoue, 1996). Consequently, the main clay
270 component varies with depth within volcanic soil deposits. Compilation of the ages of
271 volcanoclastic deposits in Japan and New Zealand (Okada et al. 1986; Lowe 1986; Inoue
272 1996) indicates that halloysite starts to $\sim 10^4$ years after deposition, which is consistent with
273 the age of the studied strata (9 ka for Ta-d). Therefore, progression of the weathering reaction
274 is likely a key process for the production of mechanically weak layers that can easily collapse
275 in volcanic areas, as observed in the present landslides.

276 Note that these inferences remain qualitative, and further work is necessary for more
277 quantitative discussion. For instance, rain water in Tomakomai city, 10 km away from Atsuma
278 town, does have Na^+ and Cl^- as its main ions species, but their concentrations fluctuate
279 (Shibata and Sakuma 1994). The presence of other cation (such as Ca^{2+} , Mg^{2+} , or K^+) and
280 anion (including SO_4^{2-} and NO_3^-) species can modify the surface physico-chemical properties
281 of the halloysite particles. Rheological measurements of halloysite suspensions have
282 demonstrated that the yield stress generally increases with decreasing pH (Theng and Wells
283 1995). This can be interpreted as a decrease in interparticle potential at lower pH (Fig. 7).
284 However, the suspension's rheology shows complicated behavior depending on NaCl
285 concentration as well as the morphology of the halloysite (Theng and Wells 1995). In-situ soil

286 monitoring would provide precise information about the way the water's ionic composition
287 changes during rainfall. In addition, future work should consider the rheological properties of
288 halloysite-bearing soil under variable chemical conditions.

289

290 **6 Conclusions**

291 The mineralogical and physico-chemical properties of the slip surface material from a landslide
292 triggered by the 2018 Hokkaido Eastern Iburi earthquake were examined. This study reached
293 the following conclusions.

294 (1) TEM observation revealed that halloysite in the slip surface exhibited irregular and
295 occasionally spherical morphology. Halloysite tubes or particles with a wood shaving-like
296 shape, as documented in previous work, were not observed here.

297 (2) Halloysite in the slip surface has higher mesopore volumes than the standard tubular sample,
298 which may be related to a high capacity of water retention after rainfall.

299 (3) To simulate possible chemical changes in soils during rainfall, samples were immersed in
300 rainwater at different S/W ratios. Increasing rainwater infiltration appeared to increase the
301 pH and decrease the EC within the slip surface.

302 (4) Electrophoretic measurements showed that the zeta potential of the slip surface material
303 behaved similarly to a standard halloysite sample, but with differences at lower pH.

304 Generally, the absolute zeta potential values increased with increasing pH and decreasing
305 solute concentration.

306 (5) Applying DLVO theory to the obtained zeta potentials derived the interparticle potential of
307 halloysite. The potential increased with decreasing solute concentration and increasing
308 absolute zeta potential. These findings collectively suggest that rainwater saturation
309 enhanced the colloidal stability of halloysite particles, and resulted in the decrease in
310 cohesive strength of the material. These physico-chemical effects might also have affected
311 the rheological properties of the volcanic soil, and led to the eventual collapse and
312 downflow of debris triggered by seismic ground motion.

313

314 **Abbreviations**

315 PSD: Particle size distribution; EC: Electrical conductivity; S/W: Solid/water weight ratios

316

317 **Declarations**

318 **Availability of data and material**

319 The datasets supporting the conclusions of this article are included within the article (and its
320 additional file.

321

322 **Competing interests**

323 The authors declare that they have no competing interest.

324

325 **Funding**

326 This work was supported by a JSPS Grant-in-Aid for Scientific Research (18H0129508).

327

328 **Authors' contributions**

329 JK designed the study, carried out the experimental study, analyzed the data and construct
330 manuscript.

331

332 **Acknowledgements**

333 I thank Shuhei Shimoda and Tatsuhiko Sigyo for technical assistance with the TEM observations
334 and water adsorption–desorption experiment. The JEM-2100F Jeol instrument is registered
335 with the Open Facility system and managed by the Global Facility Center, Creative Research
336 Institution, Hokkaido University.

337

338 **References**

339 Askenasy PE, Dixon JB, McKee TR (1973) Soil Sci Soc Am Proc 37: 799–803.

340 Barrett EP, Joyner LG, Halenda PP (1951) The Determination of Pore Volume and Area
341 Distributions in Porous Substances. I. Computations from Nitrogen Isotherms. J Am Chem
342 Soc 73: 373–380.

343 Brigatti MF, Galan E, Theng B.K.G. (2006) Structures and mineralogy of clay minerals. in: F.
344 Bergaya B.K.G. Theng, G. Lagaly (Eds.), Handbook of Clay Science, Elsevier, Amsterdam,
345 pp. 19–86.

346 Chigira M, Yokoyama O (2005) Weathering profile of non-welded ignimbrite and the water
347 infiltration behavior within it in relation to the generation of shallow landslides. Eng Geol
348 78:187–207.

349 Chigira M, Nakasuji A, Fujiwara S, Sakagami M (2012) Catastrophic Landslides of Pyroclastics
350 Induced by the 2011 off the Pacific Coast of Tohoku Earthquake. pp 139–147 in:
351 Earthquake-Induced Landslides, Proc. Int. Symp. Earthquake-Induced Landslides, Kiryu,
352 Japan, Springer.

353 Chigira M, Tajika J, Ishimaru S (2019) Landslides of pyroclastic fall deposits induced by the
354 2018 Eastern Iwate Earthquake with special reference to the weathering of pyroclastics.
355 DPRI Annuals, 62: 348–356.

356 Duran JDG, Ontiveros A, Delgado AV, Gonzalez-Caballero F (1998) Kinetics and interfacial
357 interactions in the adhesion of colloidal calcium carbonate to glass in a packed bed. Appl

376 Inoue A (1996) Solution-mediated phase transformations of clay minerals. Journal of the
377 Mineralogical Society of Japan 25: 189–197. <https://doi.org/10.2465/gkk1952.25.189>

378 Ito Y, Yamazaki S, Kurahashi T (2020) Geological features of landslides caused by the 2018
379 Hokkaido Eastern Iburi Earthquake in Japan. Geological Society, London, Special
380 Publications 501: <https://doi.org/10.1144/SP501-2019-122>

381 Iyoda F, Hayashi S, Arakawa S, John B, Okamoto M, Hayashi H, Yuan G (2012) Synthesis and
382 adsorption characteristics of hollow spherical allophane nano-particles. Appl Clay Sci 56:
383 77–83.

384 Joussein E, Petit S, Churchman J, Theng B, Righ D, Delvaux B (2005) Halloysite clay minerals
385 – a review Clay Minerals 40: 383–426.

386 Kameda J, Kamiya H, Masumoto H, Morisaki T, Hiratsuka T, Inaoi C (2019) Fluidized
387 landslides triggered by the liquefaction of subsurface volcanic deposits during the 2018
388 Iburi–Tobu earthquake, Hokkaido. Sci Rep 9:13119. [https://doi.org/10.1038/s41598-019-](https://doi.org/10.1038/s41598-019-48820-y)
389 [48820-y](https://doi.org/10.1038/s41598-019-48820-y)

390 Kasai M, Yamada T (2019) Topographic effects on frequency-size distribution of landslides
391 triggered by the Hokkaido Eastern Iburi Earthquake in 2018. Earth Planets Space 71:89
392 <https://doi.org/10.1186/s40623-019-1069-8>

393 Katsui Y (1959) On the Shikotsu pumice-fall deposit. Special reference to the activity just

394 before the depression of the Shikotsu caldera. *Bull Volcanol Soc Jpn* 2: 33–48.

395 Kawachi T, Matsuura Y, Iyoda F, Arakawa S, Okamoto M (2013) Preparation and
396 characterization of DNA/allophane composite hydrogels. *Coll Surf B: Biointerfaces* 112:
397 429–434.

398 Kluger MO, Moon VG, Kreiter S, Lowe DJ, Churchman GJ, Hepp D A, Seibel D, Jorat ME,
399 Mörz T (2017) A new attraction-detachment model for explaining flow sliding in clay-rich
400 tephras. *Geology* 45(2):131–134.

401 Lagaly G (2006) Colloid clay science. In: Bergaya, F., Theng, B.K.G., Lagaly, G. (Eds.),
402 Handbook of Clay Science. Elsevier, Amsterdam, pp. 247–260.

403 Lowe DJ (1986) Controls on the rates of weathering and clay mineral genesis in airfall tephras:
404 A review and New Zealand case study. In: S. M. Colman and D. P. Dethier, (eds.), Rates of
405 Chemical Weathering of Rocks and Minerals, Academic Press, pp. 265–330.

406 Moon V (2016) Halloysite behaving badly: geomechanics and slope behaviour of halloysite-
407 rich soils. *Clay Miner* 51:517–528.

408 Nakagawa M, Amma-Miyasaka M, Miura D, Uesawa S (2018) Tephrastratigraphy in Ishikari
409 Lowland, Southwestern Hokkaido: Eruption history of the Shikotsu-Toya volcanic field.
410 *Jour Geol Soc Jpn* 124: 473–489.

411 Nakano M, Chigira M, Choun-Sian L (2013) Landslides of pumice fall deposits induced by the

412 2009 Padang earthquake and the formation of halloysite. Japan Geosci. Union Meeting,
413 Chiba, Japan.

414 Okada K, Oosaka J, Matsui K, Suzuki M (1986) On the factors influencing the weathering of
415 tephra in various parts of Japan. *Jour Mineral Soc Jpn* 17: 25–33.

416 Osanai N, Yamada T, Hayashi S, Katsura S, Furuichi T, Yanai S, Murakami Y, Miyazaki T,
417 Tanioka Y, Takiguchi S, Miyazaki M (2019) Characteristics of landslides caused by the
418 2018 Hokkaido Eastern Iburi Earthquake. *Landslides* 16: 1517–1528,
419 <https://doi.org/10.1007/s10346-019-01206-7>

420 Parfitt RL, [Russell](#) M, [Orbell](#) GE (1983) Weathering sequence of soils from volcanic ash
421 involving allophane and halloysite, New Zealand. *Geoderma* 29 (1):41–57.

422 Plaza I, Ontiveros-Ortega A, Calero J, Romero C (2018) A new approach to triggering
423 mechanism of volcano landslides based on zeta potential and surface free energy balance.
424 *Geomorph* 301: 1–9.

425 Saeki K, Sakai M, Wada S (2010) DNA adsorption on synthetic and natural allophanes. *Appl*
426 *Clay Sci* 50: 493–497.

427 Shibata H, Sakuma T (1994) Acid Deposition at Forest Regions in North-Western Part of
428 Tomakomai. *Jpn Jour Soil Sci J Plant Nutr* 65: 313–320.

429 Sing KSW, Everett DH, Haul RAW, Moscou L, Peirotti R.A., Rouquerol J (1985). IUPAC

430 commission on colloid and surface chemistry including catalysis. *Pure Appl Chem* 57:
431 603–619.

432 Smalley I, Ross CW, Whitton J (1980) Clays from New Zealand support the inactive particle
433 theory of soil sensitivity. *Nature* 288: 576–577, doi: 10.1038/288576a0.

434 Suzuki M, Suzuki S, Maeda M, Tomura S, Mizota T (2001) Hydration rate of allophane and
435 imogolite by hydration heat measurement using as heat exchange absorbents for lower
436 temperature heat source and speedy drying desiccant. *J Ceramic Soc Jpn* 109(10): 874–881.

437 Smoluchowski MV (1921) *Handbook of Electricity and Magnetism*. Barth, Leipzig. 366.

438 Theng BKG, Wells N (1995) The flow characteristics of halloysite suspensions. *Clay Miner* 30:
439 99–106.

440 Tomura S, Maeda M, Inukai K, Ohashi F, Suzuki M, Shibasaki Y, Suzuki S (1997) Water vapor
441 adsorption property of various clays and related materials for applications to humidity self-
442 control materials. *Clay Sci* 10: 195–203.

443 Van Olphen H (1977) *An Introduction to Clay Colloid Chemistry*. Wiley, New York, USA.

444 Vergaro V, Abdullayev E, Lvov YM, Zeitoun A, Cingolani R, Rinaldi R, Leporatti S (2010)
445 Cytocompatibility and uptake of halloysite clay nanotubes. *Biomacromolecules* 11(3):
446 820–826.

447 Wada K (1977) *Minerals in Soil Environments*. Soil Sci Soc Am Madison, Wisconsin, 603.

448 Wada K, Mizota C (1979) The Clay Science Society of Japan, 42.

449 Wada K (1980) Soils with Variable Charge. New Zealand Society of Soil Science, Lower Hutt,
450 87.

451 WADA K (1989) Allophane and Imogolite, in Minerals in Soil Environments (2nd ed) Soil
452 Science Society of America, SSSA Book Series, 1, pp 1051–1087.

453 Wang S, Du P, Yuan P, Liu Y, Song H, Zhou J, Deng L, Liu D (2020) Structural alterations of
454 synthetic allophane under acidic conditions: Implications for understanding the
455 acidification of allophanic Andosols. *Geoderma* 376:114561.
456 <https://doi.org/10.1016/j.geoderma.2020.114561>

457 Yamada S (1958) Studies on the history of volcanic eruptions of alluvium epoch in Hokkaido
458 on the basis of depositional features of the pyroclastics. *Monog Ass Geol Collab Jpn* 8.

459 Yamagishi H, Yamazaki F (2018) Landslides by the 2018 Hokkaido Iburi-Tobu Earthquake on
460 September 6. *Landslides* 15: 2521–2524.

461

462 **Figure legends**

463 Figure 1. Location and occurrence of the studied landslide. (a) Locations of the epicenter of the
464 Eastern Iburi earthquake (red cross) and the study area. (b) 3D view of the hills near Atsuma
465 after the earthquake (produced by data from the Geographical Survey Institute, 2018a). (c)

466 Close-up photograph of the studied landslide (taken on 6 September 2018; Geographical Survey
467 Institute, 2018b). (d) Striated mud on the collapsed slope (modified after Kameda et al. 2019).
468 (e) Scarp measuring 2–3 m in height, which contains a stratigraphic sequence of volcanoclastic
469 deposits (modified after Kameda et al. 2019).

470

471 Figure 2. Bulk XRD pattern of the slip surface material with a corundum internal standard.

472

473 Figure 3. TEM micrograph of halloysite in the slip surface. The particle indicated by the arrow
474 is a hollow sphere.

475

476 Figure 4. Results of the N₂ adsorption–desorption experiments. (a) N₂ adsorption–desorption
477 isotherms for the slip surface material, halloysite, and allophane. (b) Pore size distribution
478 (PSD) curves obtained from BJH analysis.

479

480 Figure 5. Water adsorption–desorption isotherms at 25 °C for the slip surface material,
481 halloysite, and allophane.

482

483 Figure 6. Results of immersion tests. Changes in pH and electrical conductivity after sample

484 immersion for 24 h in rainwater or distilled water (DW) at different solid/water weight ratios.

485

486 Figure 7. Results of electrophoretic analysis. (a) Zeta potentials with respect to pH. Results for
487 standard halloysite and allophane samples are included for comparison. (b) Zeta potentials with
488 respect to pH at different solute concentrations. Error bars denote the range of three repeated
489 measurements.

490

491 Figure 8. Hydrodynamic diameter of particles (nm). The diameter was measured by dynamic
492 light scattering as a function of solute concentration. Error bars denote the range of three
493 repeated measurements.

494

495 Figure 9. Interparticle potential (in kT) based on DLVO theory. (a) The zeta potential was set at
496 -35 mV. (b) The solute concentration was set as 5.0×10^{-4} M.

497

498 **Tables**

499 Table 1. Specific surface area and total pore volume of the slip surface material, standard
500 halloysite, and allophane

501

Figures

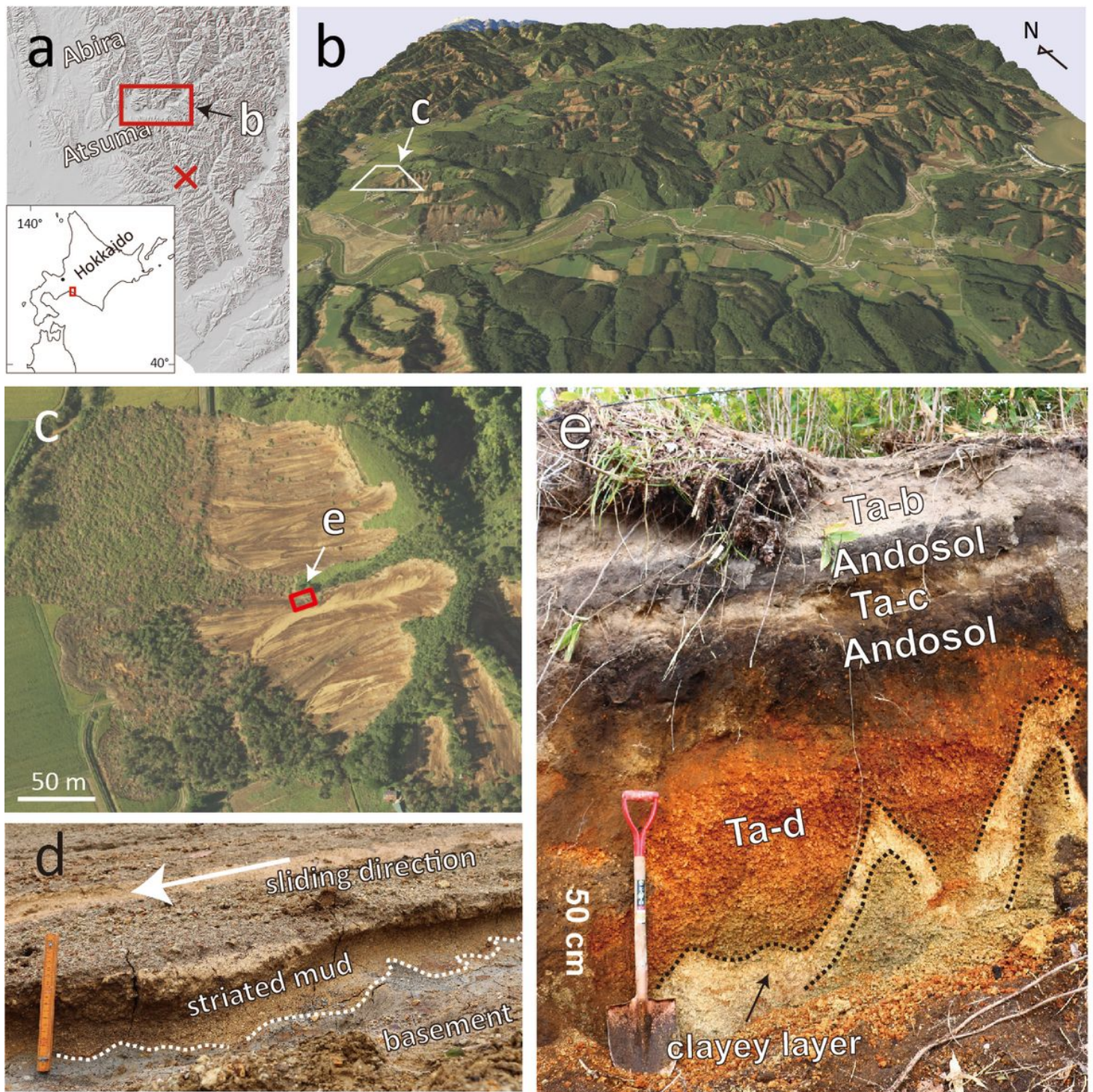


Figure 1

Location and occurrence of the studied landslide. (a) Locations of the epicenter of the Eastern Iburi earthquake (red cross) and the study area. (b) 3D view of the hills near Atsuma after the earthquake (produced by data from the Geographical Survey Institute, 2018a). (c) Close-up photograph of the studied landslide (taken on 6 September 2018; Geographical Survey Institute, 2018b). (d) Striated mud on the

collapsed slope (modified after Kameda et al. 2019). (e) Scarp measuring 2–3 m in height, which contains a stratigraphic sequence of volcanoclastic deposits (modified after Kameda et al. 2019).

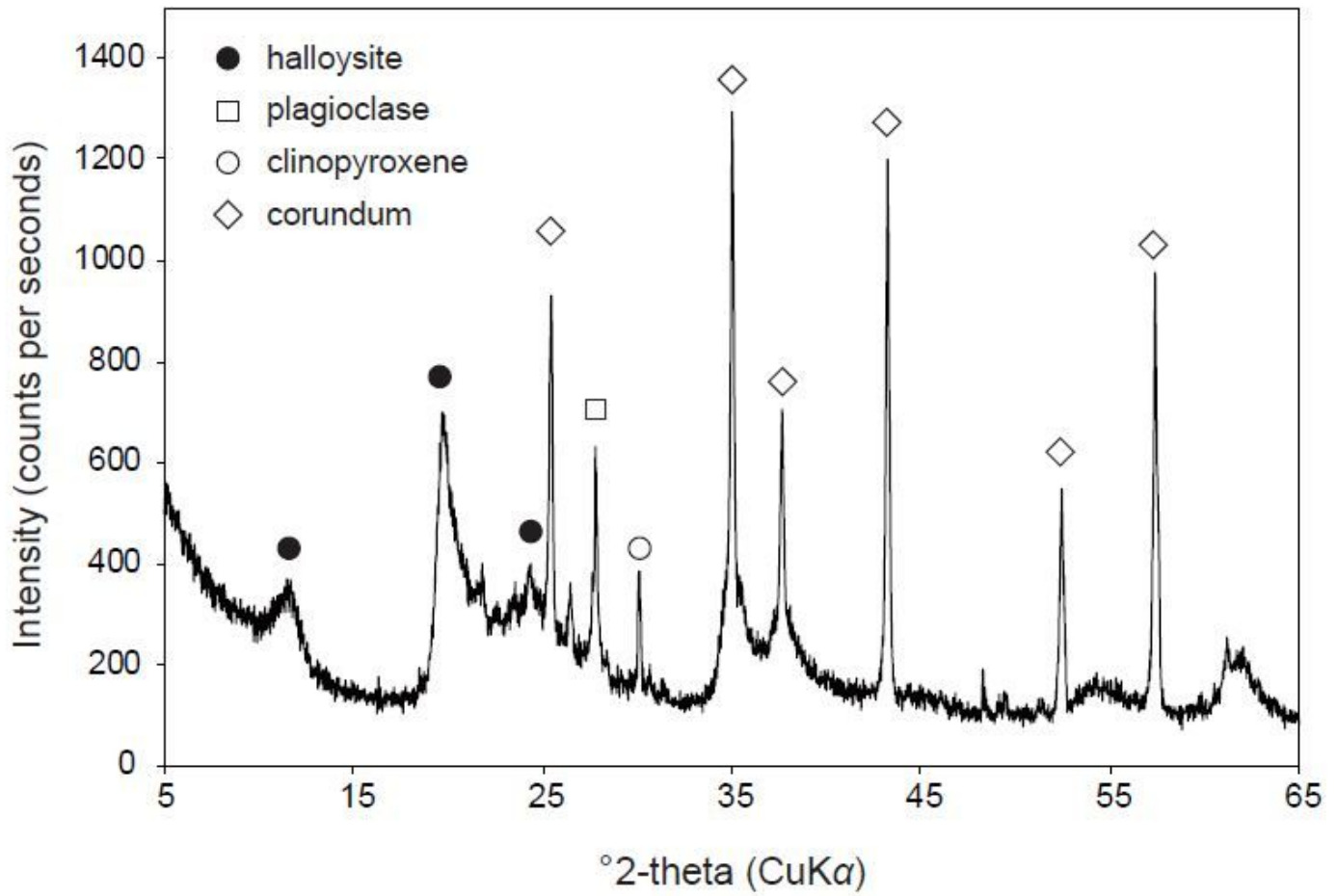


Figure 2

Bulk XRD pattern of the slip surface material with a corundum internal standard.

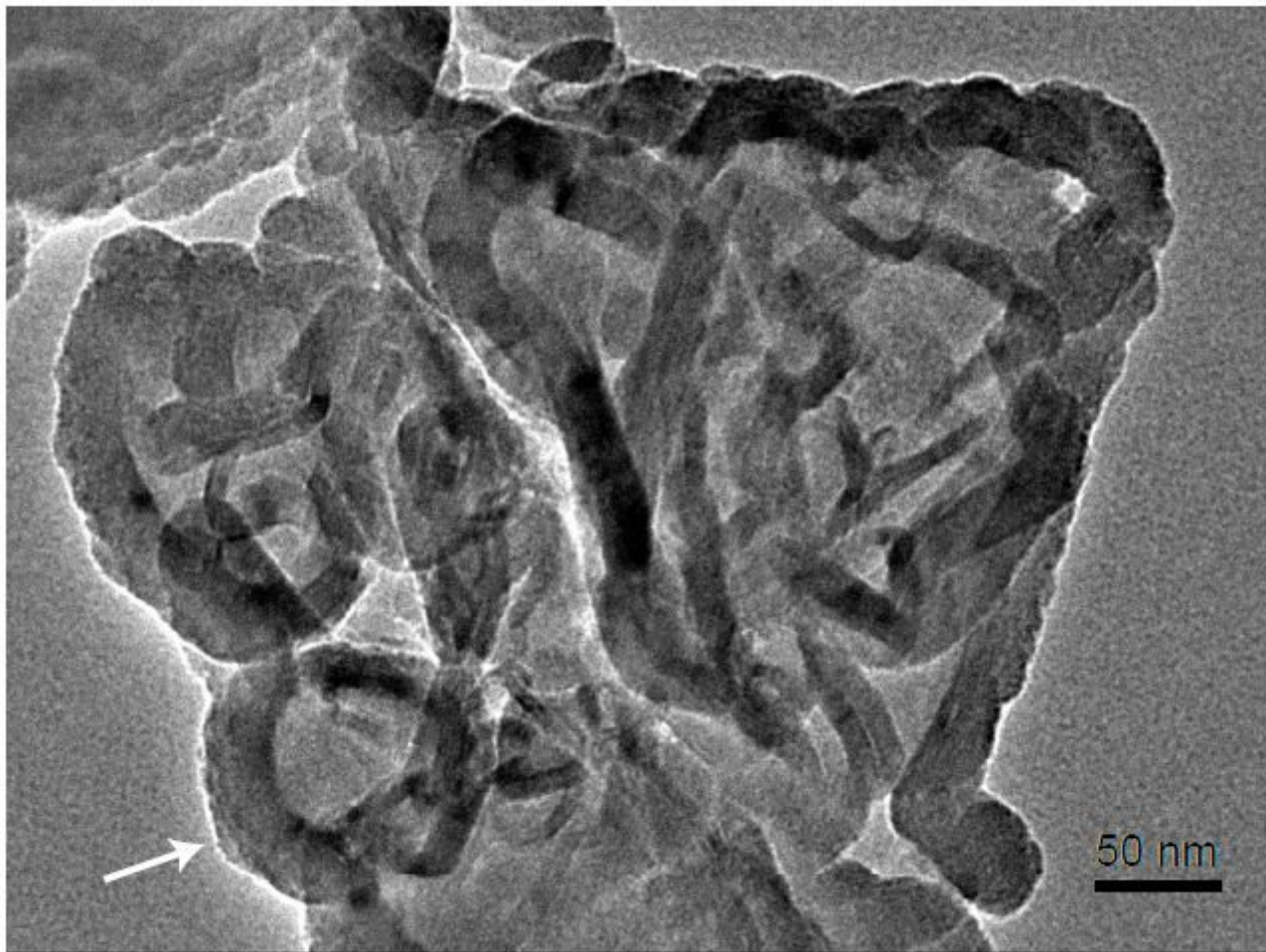


Figure 3

TEM micrograph of halloysite in the slip surface. The particle indicated by the arrow is a hollow sphere.

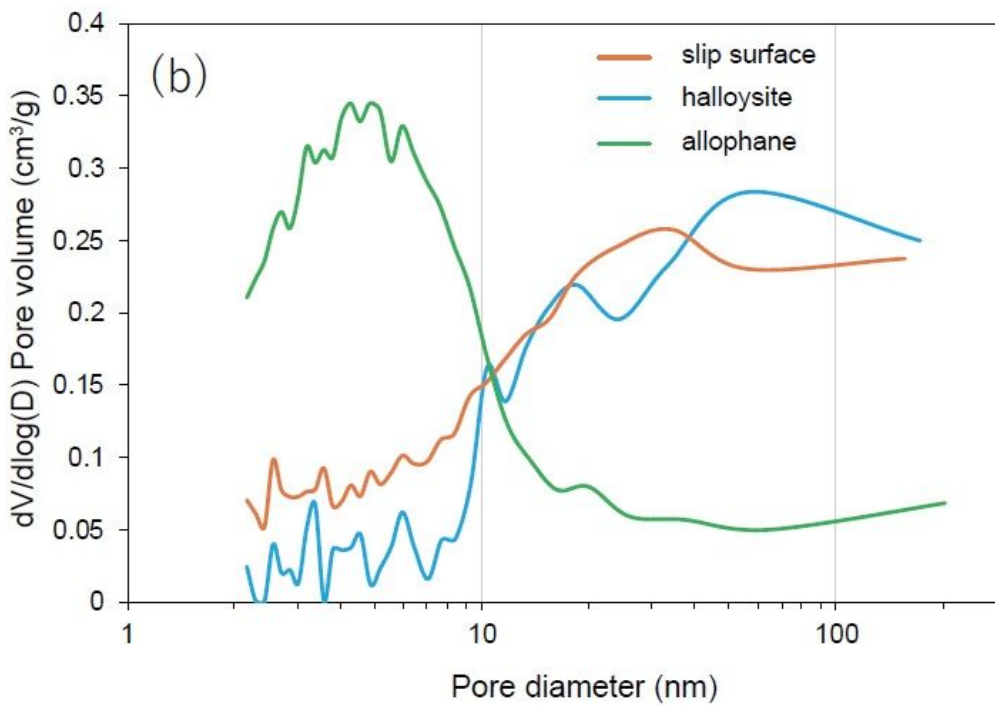
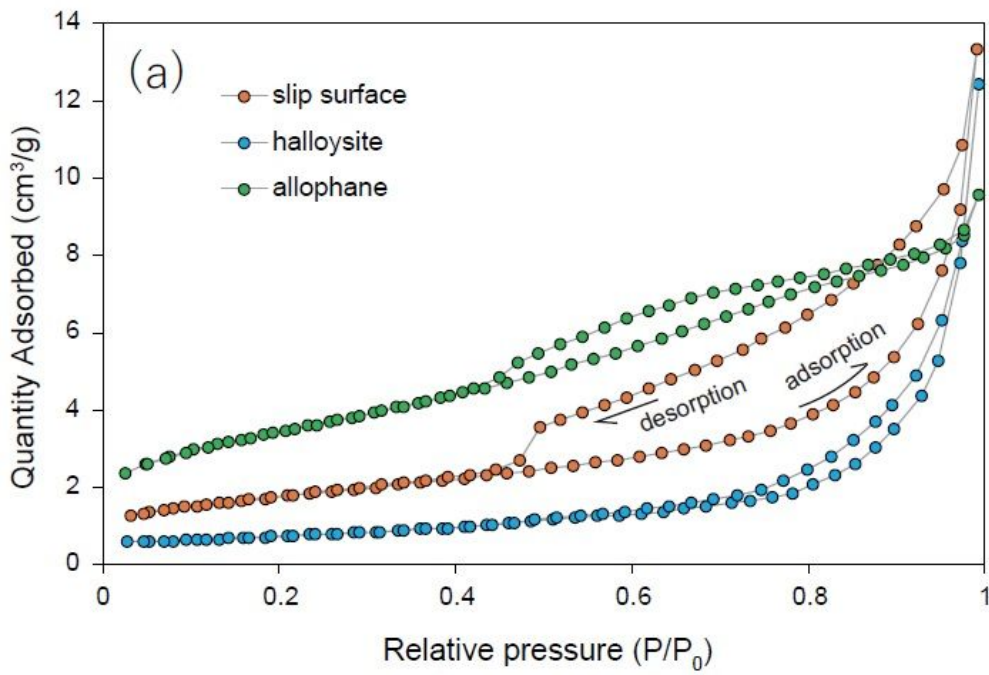


Figure 4

Results of the N₂ adsorption–desorption experiments. (a) N₂ adsorption–desorption isotherms for the slip surface material, halloysite, and allophane. (b) Pore size distribution (PSD) curves obtained from BJH analysis.

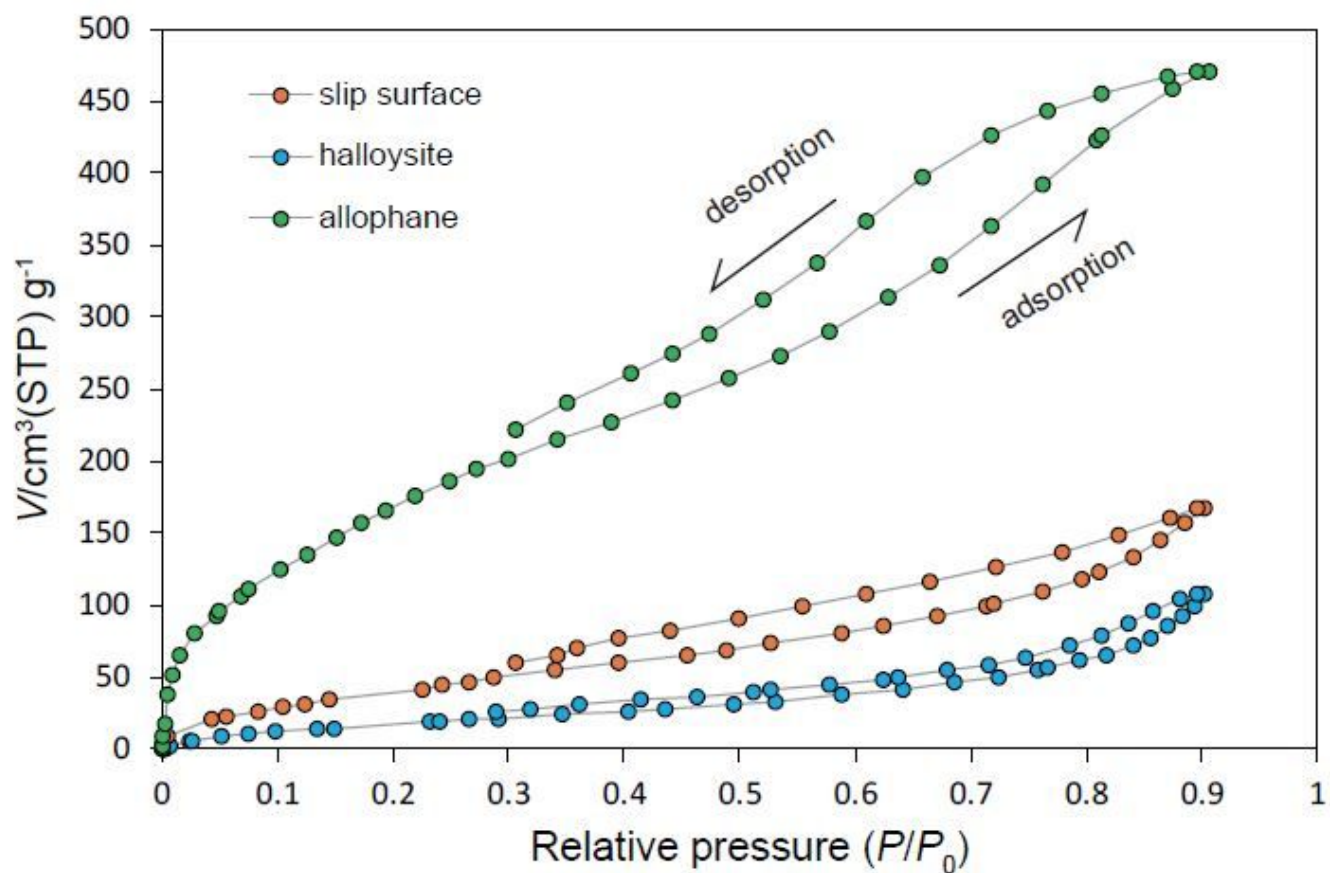


Figure 5

Water adsorption-desorption isotherms at 25 °C for the slip surface material, halloysite, and allophane.

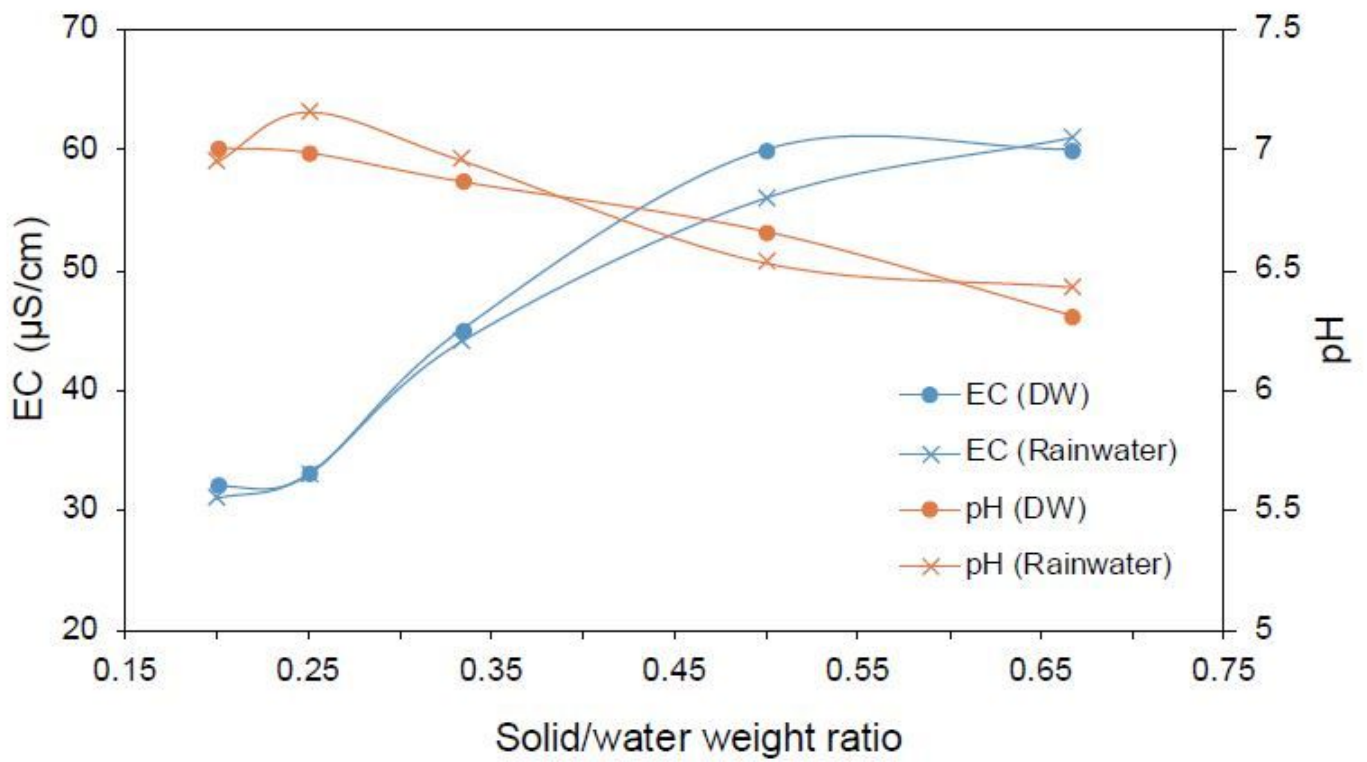


Figure 6

Results of immersion tests. Changes in pH and electrical conductivity after sample immersion for 24 h in rainwater or distilled water (DW) at different solid/water weight ratios.

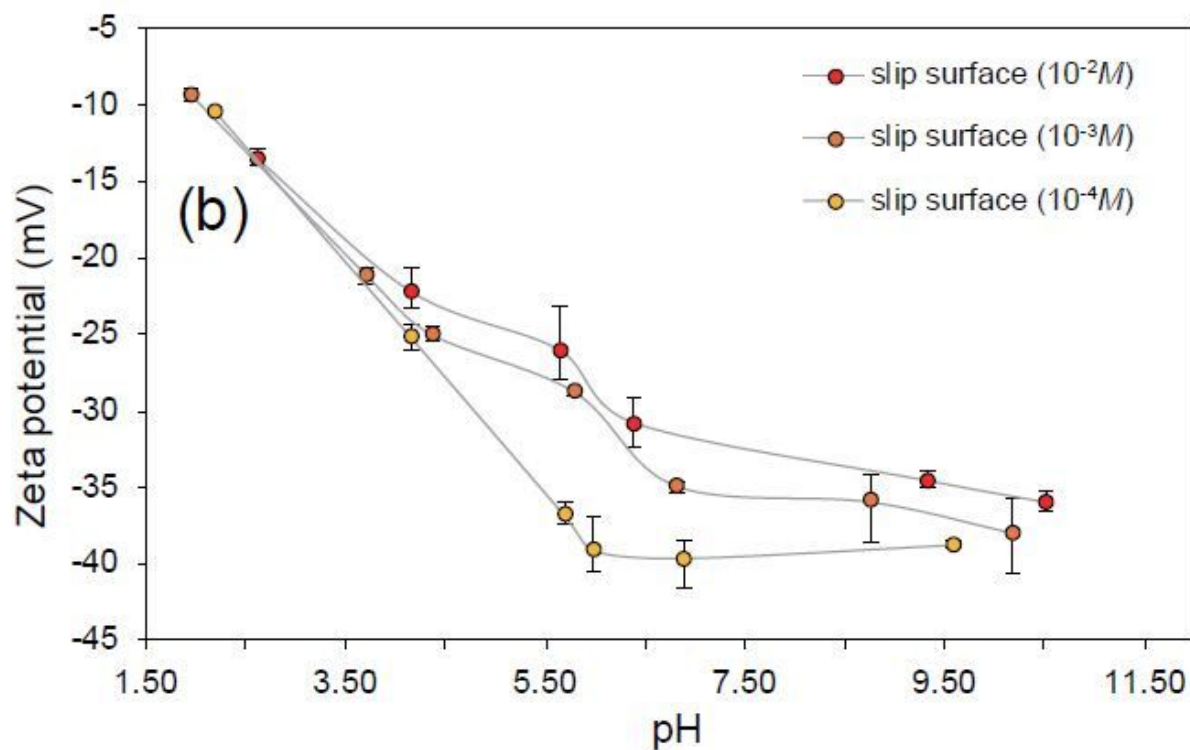
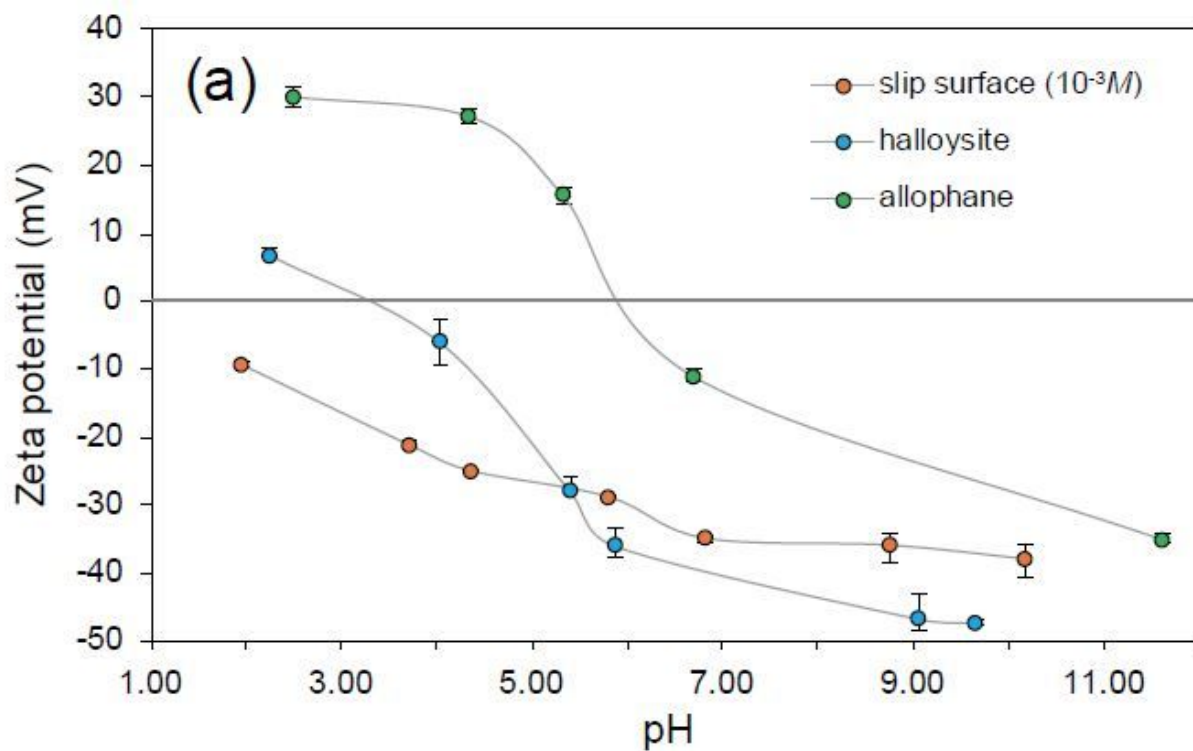


Figure 7

Results of electrophoretic analysis. (a) Zeta potentials with respect to pH. Results for standard halloysite and allophane samples are included for comparison. (b) Zeta potentials with respect to pH at different solute concentrations. Error bars denote the range of three repeated measurements.

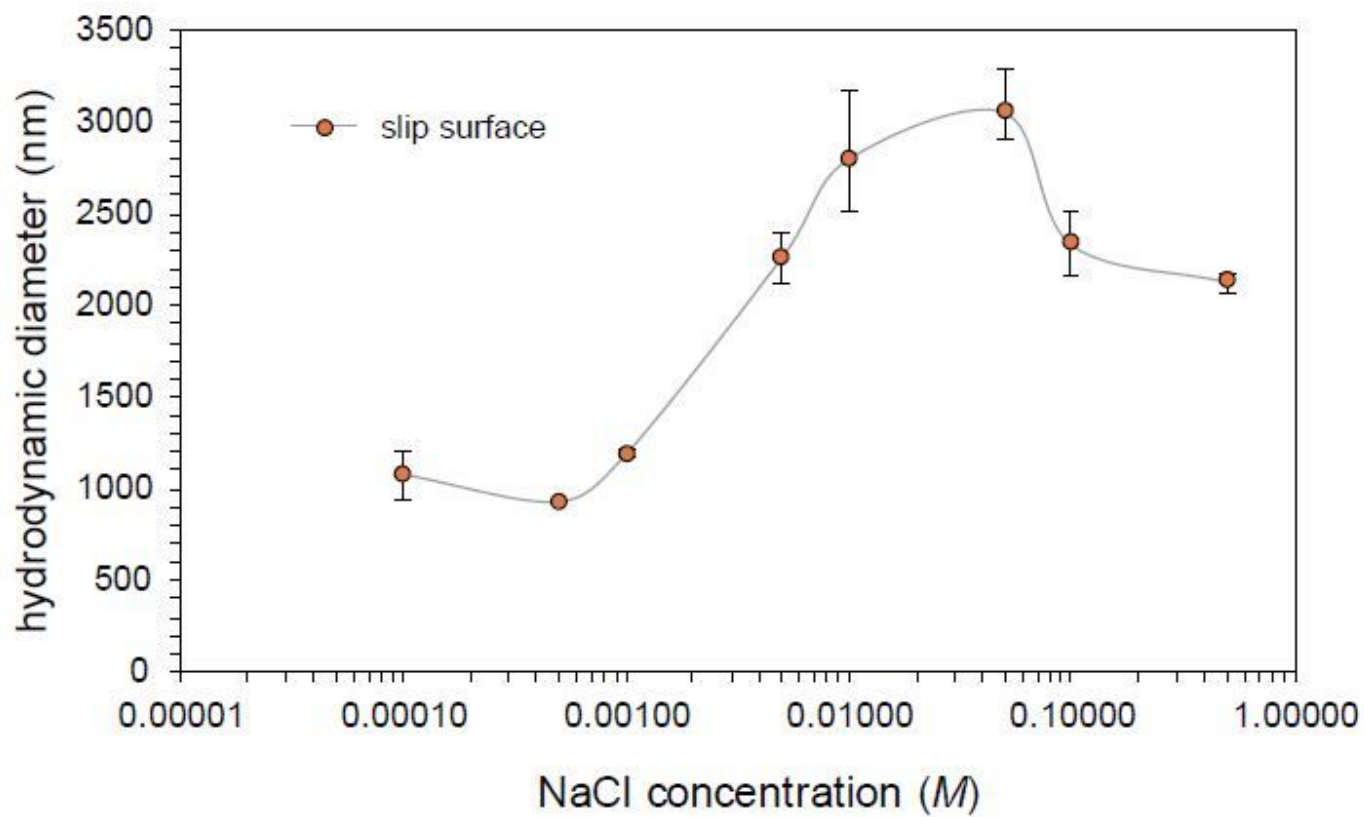


Figure 8

Hydrodynamic diameter of particles (nm). The diameter was measured by dynamic light scattering as a function of solute concentration. Error bars denote the range of three repeated measurements.

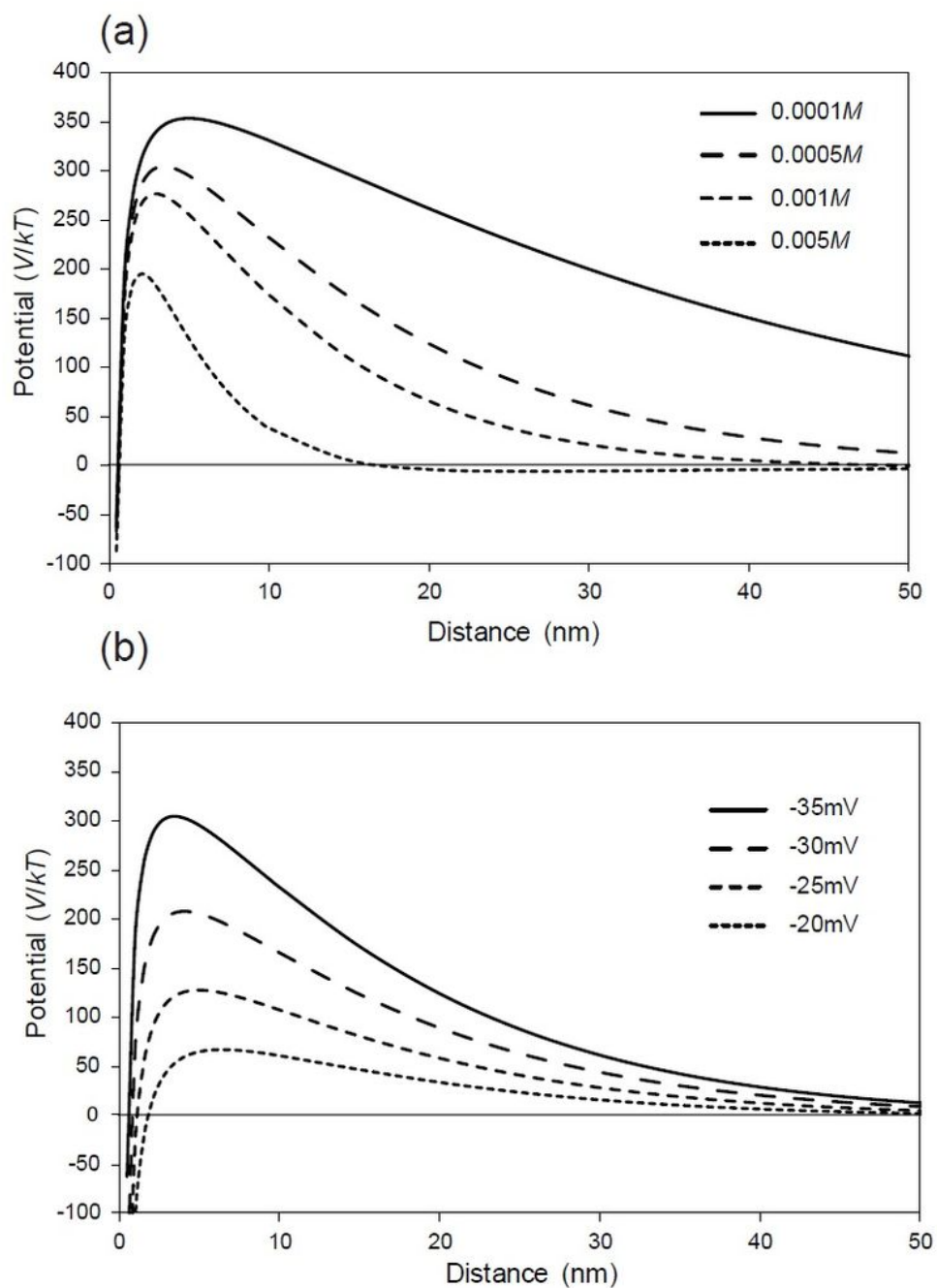


Figure 9

Interparticle potential (in kT) based on DLVO theory. (a) The zeta potential was set at -35 mV . (b) The solute concentration was set as $5.0 \times 10^{-4}\text{ M}$.

Supplementary Files

This is a list of supplementary files associated with this preprint. Click to download.

- [Table1.pdf](#)